Impingement of a propeller-slipstream on a leading edge with a flow-permeable insert
A computational aeroacoustic study

Avallone, Francesco; Casalino, Damiano; Ragni, Daniele

DOI
10.1177/1475472X18788961

Publication date
2018

Document Version
Final published version

Published in
International Journal of Aeroacoustics

Citation (APA)
Avallone, F., Casalino, D., & Ragni, D. (2018). Impingement of a propeller-slipstream on a leading edge with a flow-permeable insert: A computational aeroacoustic study. *International Journal of Aeroacoustics*, *17*(6-8), 687-711. https://doi.org/10.1177/1475472X18788961

Article

aeroacoustics

International Journal of Aeroacoustics
2018, Vol. 17(6–8) 687–711

DOI: 10.1177/1475472X18788961
journals.sagepub.com/home/jae
SAGE

Impingement of a propeller-slipstream on a leading edge with a flow-permeable insert: A computational aeroacoustic study

Francesco Avallone, Damiano Casalino and Daniele Ragni

Abstract

This manuscript describes an aeroacoustic computational study on the impingement of a tractor-propeller slipstream on the leading edge of a pylon. Both the flow and acoustic fields are studied for two pylon leading edges: a solid and a flow-permeable one. The computational set-up replicates experiments performed at Delft University of Technology. Computational results are validated against measurements. It is found that the installation of the flow-permeable leading-edge insert generates a thicker boundary layer on the retreating blade side of the pylon. This is caused by an aerodynamic asymmetry induced by the helicoidal motion of the propeller wake, which promotes a flow motion through the cavity from the advancing to the retreating blade side of the pylon. The flow-permeable leading-edge insert mitigates the amplitude of the surface pressure fluctuations only on the pylon-retreating blade side towards the trailing edge, thus reducing structure-borne noise. Furthermore, it causes a reduction of the near-field noise only for receiver angles oriented in the upstream direction at the pylon-retreating blade side. In this range of receiver angles, it is found that the flow-permeable leading-edge insert reduces the amplitude of the tonal peaks for the third and fourth blade passage frequency, but strongly increases the broadband noise for frequencies higher that the seventh blade passage frequency.

Keywords

Flow-permeable leading edge, tractor-propeller noise, vortex-impingement noise

Date received: 15 December 2017; accepted: 30 May 2018

AWEP Department, Delft University of Technology, Delft, The Netherlands

Corresponding author:
Francesco Avallone, AWEP Department, Wind Energy Section, Delft University of Technology, Kluyverweg 1, 2629HS Delft, The Netherlands.
Email: f.avallone@tudelft.nl

Introduction

Propellers are an interesting propulsion system because of the lower fuel consumption of about 10–20% with respect to turbofan engines,[1] and for the recent focus on electric propulsion. On the other side, propellers generate higher noise that reduces cabin comfort. To minimize cabin noise, propellers are positioned as far away as possible from the passengers[2] such as in the aft-mounted propeller configuration, where the propeller is connected to the airframe through a dedicated pylon. In this case, propellers can be mounted in a tractor or pusher configuration. From an acoustic point of view, the latter suffers for an additional noise source due to the unsteady impingement of the pylon wake on the propeller blades.[3,4] To avoid this source of noise, propellers can be mounted in a tractor configuration.

Aft-mounted tractor-propeller configurations show two distinct effects: an upstream effect, due to the presence of the pylon that perturbs the propeller inflow; and a downstream effect, due the propeller slipstream impinging on the pylon that reduces the pylon aerodynamic performance. The upstream disturbance of the propeller inflow leads to a non-uniform blade loading, introducing an additional noise source next to the steady-loading and thickness noise generated by the isolated propeller.[5] However, at low angles of attack, the upstream effect is negligible with respect to the downstream one particularly for pylon-mounted configurations featuring symmetric profiles.[6]

The periodic impingement of the rotor blade wakes and tip vortices is experienced by the pylon as an unsteady inflow condition, resulting in an unsteady loading with span-wise and chord-wise gradients.[7–10] The unsteady pylon loads cause vibrations, which are transmitted into the structure of the aircraft and can be perceived by the passengers as structure-borne noise.[11] This noise source can be mitigated by modifying the transmission path of the vibrations,[12] or by decreasing the amplitude of the unsteady aerodynamic loading. A possible way to reduce the amplitude of the unsteady loading is to use a pylon with a flow-permeable leading edge, also referred to as passive porosity.[13–16] Tinetti et al.[13,14] applied passive porosity to mitigate the unsteady loading for rotor–stator interaction in turbomachinery. They showed a reduction of the unsteady loading up to 21%. However, it was shown that the flow-permeable leading edge modifies the pressure distribution on the surface, thus changing the effective aerodynamic shape. Lee[15] applied a flow-permeable leading edge for blade–vortex interaction noise for helicopter applications, showing a reduction of the amplitude of the interaction noise up to 30%. Della Corte et al.[16] investigated experimentally the potential of flow-permeable leading edges to alleviate the unsteady loading caused by the impingement of the propeller slipstream on a downstream surface, for which wake-impingement and vortex-impingement phenomena occur simultaneously. The spatial distribution of the cavities was based on the optimal configuration identified by Tinetti et al.[13,14] They investigated the effect of both the cavity size and of the hole diameter with particle image velocimetry (PIV). The experiments showed that the near-wall pressure fluctuations decrease up to 30% at the tip-vortex impingement region, thus reducing the unsteady loading up to 25%. On the other side, they showed large penalties in terms of aerodynamic performances (i.e. lower lift and higher drag), in particular at angles of attack higher than 6°. This is caused by the larger boundary-layer thickness on the retreating blade side of the pylon due to the cross-flow through the flow-permeable leading edge.

The turbulent boundary layer developing over the aerofoil and the cross-flow through the holes can affect the near- and far-field noise and its directivity because of two noise sources:

leading-edge impingement noise and the turbulent-boundary-layer trailing-edge noise. To the authors' knowledge, no analysis on the cavity flow and on the far-field noise for a flow-permeable leading-edge insert has been carried out in the literature. For this reason, and because many studies on flow-permeable materials at the leading edge have been presented in the recent literature,[17,18] a computational investigation of both the flow and acoustic fields for a flow-permeable leading edge has been carried out. The flow is computed by solving the explicit, transient, compressible Lattice-Boltzmann (LB) equation, while the acoustic field is obtained by means of the Ffowcs Williams and Hawkings (FWH) acoustic analogy.[19] The configuration replicates the experiments performed at Delft University of Technology,[9,10,16] which are used as benchmark.

In the following article, initially, the computational method and set-up are discussed. The grid-convergence study and the comparison with the experiments are presented next. The flow field and the acoustic footprint are then discussed. A summary of the findings is reported in the concluding section.

Computational method

Flow solver

The LB method is used to compute the flow field because it was shown to be accurate and efficient for noise prediction in presence of complex flow problems.[20–24] The commercial software PowerFLOW 5.4a is used. The software solves the discrete LB equation for a finite number of directions. For a detailed description of the method, the reader can refer to Succi[25] and Shan et al.,[26] while to Chen and Doolen[27] for a review. The LB method determines the macroscopic flow variables starting from the mesoscopic kinetic equation, i.e. the LB equation. The discretization used for this particular application consists of 19 discrete velocities in three dimensions (D3Q19), involving a third-order truncation of the Chapman-Enskog expansion. It was shown that this scheme accurately approximates the Navier-Stokes equations for a perfect gas at low Mach number in isothermal conditions.[28] The distribution of particles is solved by means of the LB equation on a Cartesian mesh, known as a lattice. An explicit time integration and a collision model are used. The LB equation can then be written as

$$g_i(\mathbf{x} + \mathbf{c}_i \Delta t, t + \Delta t) - g_i(\mathbf{x}, t) = C_i(\mathbf{x}, t) \tag{1}$$

where g_i is the particle distribution function along the ith lattice direction. It statistically describes the particle motion at a position $\mathbf{x}$ with a discrete velocity $\mathbf{c}_i$ in the ith direction at time t. $\mathbf{c}_i \Delta t$ and Δt are space and time increments, respectively. $C_i(\mathbf{x}, t)$ is the collision term for which the Bhatnagar-Gross-Krook model[28,29] is adopted because of its simplicity and stability

$$C_i(\mathbf{x}, t) = -\frac{\Delta t}{\tau} \left[g_i(\mathbf{x}, t) - g_i^{\mathrm{eq}}(\mathbf{x}, t) \right] \tag{2}$$

where τ is the relaxation time and g_i^{eq} is the local equilibrium distribution function. For small Mach number flows, the equilibrium distribution of Maxwell-Boltzmann is conventionally used.[28] It is approximated by a second-order expansion as

$$g_i^{\mathrm{eq}} = \rho\,\omega_i\left[1 + \frac{\mathbf{c}_i\mathbf{u}}{c_s^2} + \frac{(\mathbf{c}_i\mathbf{u})^2}{2c_s^4} + \frac{|\mathbf{u}|^2}{2c_s^2}\right] \tag{3}$$

where ω_i are the fixed weight functions, dependent on the velocity discretization model D3Q19,[28] and $c_s = \frac{1}{\sqrt{3}}$ is the dimensionless speed of sound in lattice units. The macroscopic flow quantities, density ρ and velocity $\mathbf{u}$, are obtained by discrete integration of the microscopic quantities weighted by the distribution function over the state space

$$\rho(\mathbf{x}, t) = \sum\nolimits_i g_i(\mathbf{x}, t), \quad \rho\mathbf{u}(\mathbf{x}, t) = \sum\nolimits_i \mathbf{c}_i g_i(\mathbf{x}, t) \tag{4}$$

The dimensionless kinematic viscosity ν is related to the relaxation time following Chen et al.[28]

$$\nu = c_s^2\left(\tau - \frac{\Delta t}{2}\right) \tag{5}$$

A very large eddy simulation model is implemented to take into account the effect of the sub-grid unresolved scales of turbulence. Following Yakhot and Orszag,[30] a two-equation $k - \epsilon$ renormalization group is used to compute a turbulent relaxation time that is added to the viscous relaxation time

$$\tau_{\mathrm{eff}} = \tau + C_\mu \frac{k^2/\epsilon}{(1+\eta^2)^{1/2}} \tag{6}$$

where $C_\mu = 0.09$ and η are a combination of the local strain $\left(\eta_s = k|S_{ij}|/\epsilon\right)$, local vorticity $\left(\eta_\omega = k|\omega_{ij}|/\epsilon\right)$ and local helicity parameters.[31] The term η allows to mitigate the sub-grid scale viscosity in the presence of large resolved vortical structures.

In order to reduce the computational cost, a pressure-gradient-extended wall-model (PGE-WM) is used to approximate the no-slip boundary condition on solid walls.[32,33] The model is based on the extension of the generalized law-of-the-wall model[34] to take into account the effect of pressure gradient. The expression of the PGE-WM is

$$u^+ = \frac{1}{\kappa}\ln\left(\frac{y^+}{A}\right) + B \tag{7}$$

where

$$B = 5.0, \quad \kappa = 0.41, \quad y^+ = \frac{u_\tau y}{\nu} \tag{8}$$

and where A is a function of the pressure gradient. It captures the physical consequence that the velocity profile slows down and so expands, due to the presence of the pressure gradient, at least at the early stage of the development. The expression of A is

$$A = 1 + \frac{f\left|\frac{\mathrm{d}p}{\mathrm{d}s}\right|}{\tau_w}, \quad \widehat{\mathbf{u}}_\mathbf{s} \cdot \frac{\mathrm{d}p}{\mathrm{d}s} > 0 \tag{9}$$

$$A = 1, \quad \text{otherwise} \tag{10}$$

In the equations, τ_w is the wall shear stress, $\mathrm{d}p/\mathrm{d}s$ is the stream-wise pressure gradient, $\widehat{\mathbf{u}}_\mathbf{s}$ is the unit vector of the local slip velocity and f is a length scale equal to the size the unresolved near-wall region. These equations are iteratively solved from the first cell close to the wall in order to specify the boundary conditions of the turbulence model. For this purpose, a slip algorithm,[27] obtained as generalization of a bounce-back and specular reflection process, is used.

Noise computations

The compressible and time-dependent nature of the transient computational fluid dynamics solution together with the low dissipation and dispersion properties of the LB scheme[35] allow extracting the sound pressure field directly in the near-field up to a cut-off frequency corresponding to approximately 15 voxels per acoustic wavelength.

In the far field, noise is computed by using the FWH equation.[19] The formulation 1A, developed by Farassat and Succi[36] and extended to a convective wave equation is used in this study.[35,37] The formulation is implemented in the time domain using a source-time dominant algorithm.[38] Integrations are performed on the surface of the model where the unsteady pressure is recorded with the highest frequency rate available on the finest mesh resolution level (referred to as solid formulation). As a consequence, acoustic monopoles and dipoles distributed on the surface of the aerofoil are the only source terms of interest,[39] and the non-linear contribution related to the turbulent fluctuations in the wake of the aerofoil are neglected. For validation purposes (Validation of the computational set-up section), integration is also performed on an FWH flow permeable surface (black sphere in Figure 1). In the following, this method is named as permeable formulation.

Computational set-up

The computational test case replicates the experiments of de Vries et al.,[9] Sinnige et al.,[10] and Della Corte et al.,[16] where a tractor-propeller configuration is realized by positioning a pylon downstream of a propeller, as shown in Figure 2.

The propeller has four blades and a diameter D equal to 0.237 m. The blade angle relative to the chord at 75% of the propeller radius ($r/R = 0.75$, where r is the local radial location and R is the propeller radius) is 23.9°. Additional details of the propeller geometry are reported by de Vries et al.[9] The pylon features a straight wing with an NACA 0012 aerofoil cross-section. The pylon chord length c is 0.200 m and the span b is 0.592 m. The leading edge of the pylon is located at 0.100 m from the propeller center, corresponding to an axial spacing of 0.42 D. Two leading-edge geometries are investigated: the baseline clean leading edge (named also solid leading edge) and a flow-permeable one. The flow-permeable insert

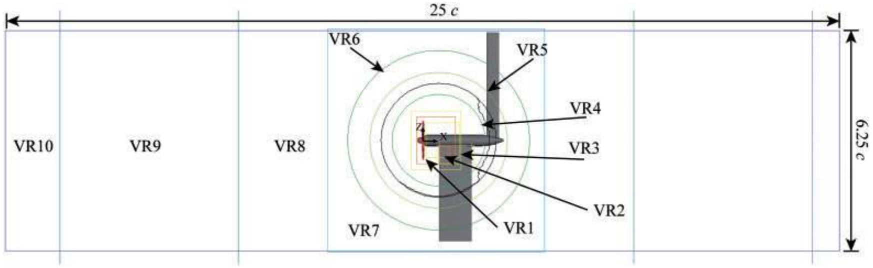

Figure 1. Side view of the computational domain with the resolution regions (VR). The resolution increases from blue to red.

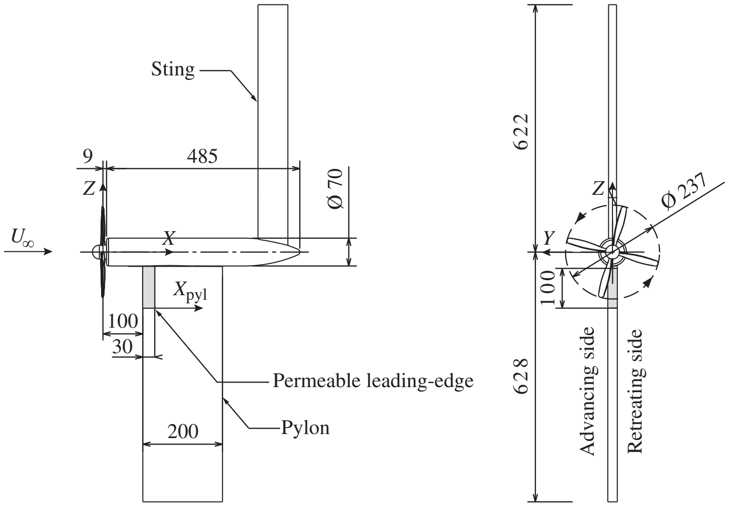

Figure 2. Geometry of the tractor-propeller configuration. Dimensions are in mm.

has a chord of 0.020 m (0.10 c) and a span of 0.100 m, and it extends up to 19% of the propeller radius below the tip of the propeller. The flow-permeable insert has a perforated skin of 1 mm thickness that covers an empty cavity underneath, as sketched in Figure 3. The stream-wise distribution of the pores is such that the permeability σ_p, defined as the ratio between open and closed surface area, is constant and equal to 0.22 for $0 \leq X_{pyl}/c \leq 0.05$, after which it decreases elliptically down to $\sigma_p = 0.10$ in the range $0.05 \leq X_{pyl}/c \leq 0.10$, where X_{pyl} is the stream-wise position along the pylon chord. This results in about nine holes along the chord for each airfoil side. The distribution is the same as in the experiments, based upon the porosity distribution proposed by Tinetti et al.[13,14] This distribution was the one that, for rotor-stator interaction, showed the best compromise between unsteady-load reductions and time-averaged aerodynamic penalties of the pylon. The hole diameter D_{hole} and the cavity thickness t_{cavity} are 1 mm and 3 mm, respectively.

The free-stream velocity U_∞ and the free-stream turbulence are set, respectively, to 40 m/s and 0.1%, as in the experiments. The pylon chord-based Reynolds number is about 550,000.

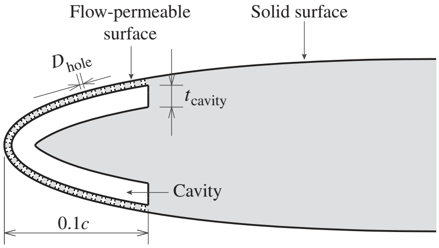

Figure 3. Geometry of the flow-permeable leading-edge insert.

The angle of attack is $\alpha = 0°$. The propeller operating condition features a rotation frequency of $n = 211.9$ Hz, resulting in an advance ratio of $J = U_\infty n^{-1} D^{-1} = 0.8$ and blade passage frequency (BPF) of about 848 Hz. The direction of rotation is shown in Figure 2 (right).

Two reference systems are used: a global reference system (X, Y, Z) and a pylon-based reference system ($X_{pyl}, Y_{pyl}, Z_{pyl}$), both shown in Figure 2. The former has origin at the centre of the propeller; the X-axis oriented in the axial direction (i.e. the free-stream direction), the Z-axis in the wall-normal direction, and the Y-axis is such to have a right-hand oriented reference system. The pylon-based reference system has origin $X_{pyl} = 0$ at the leading edge of the pylon, $Z_{pyl} = 0$ at $Z/R = -1.19$. This reference system has the same orientation as the previous one, as shown in the figure.

The simulation domain is a box of length equal to 25 c (5 m) in the X direction, 6.25 c (1.25 m) in the Z direction and 9 c (1.8 m) in the Y direction, as the wind-tunnel test section. Slip boundary conditions are imposed on all the sides of the computational domain. Outside a circular refinement zone of diameter equal to 5 c, an anechoic outer layer is used to damp-out the outward radiating and the inward reflected acoustic waves. It has been verified, through visualization of the dilatation plot, that this does not trigger any acoustic reflection. A total of 10 mesh refinement regions (VR) with resolution factor equal to 2 are employed. They are shown in Figure 1, where colors from blue to red correspond to resolution increase. The minimum voxel size is about 0.07 mm (i.e. 14 voxels/D_{hole}) and it is used to discretize the flow field around the blades, the hub and the holes of the flow permeable surface. The rest of the leading edge and the pylon are modelled with one coarser level of resolution. The corresponding dimensionless wall distance $y+$ is reported in Figure 4. In total, about 7.5×10^8 voxels (vx) and 1.15×10^7 surfels are used to discretize the problem. The flow-simulation time is equal to eight rotor revolutions (0.037 s) requiring 2.36×10^3 CPU hours per revolution on a Linux Xeon E5–2690 2.9 GHz platform.

The physical time step, corresponding to a Courant-Friedrichs-Lewy number of 1 in the finest mesh resolution level, is 1.13×10^{-7} s. Surface pressure fluctuations are sampled with a frequency of $f = 20$ kHz ($St_c = fc/u_\infty = 100$, $f/\text{BPF} \approx 24$) for a physical time of 0.0237 s (equals to five rotor revolutions).

Validation of the computational set-up

Computational results are validated through a grid-convergence study and against experimental data. The grid-resolution study is carried out to verify that both the fluid-dynamic results and the acoustic field do not depend on the chosen grid. This is achieved by

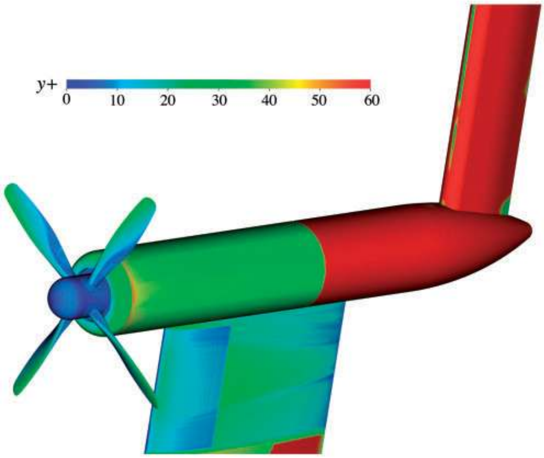

Figure 4. Dimensionless wall distance $y+$ for the grid resolution of 14 voxels/D_{hole}.

uniformly increasing the resolution of each refinement region. Four grid resolutions are investigated with minimum voxel size, respectively, equal to 5, 10, 14, 20 vx$/D_{hole}$. The rotor thrust coefficient C_T is the integral parameter used for the comparison. It is defined as

$$C_T = T\rho_\infty^{-1} n^{-2} D^{-4} \tag{11}$$

where T is the rotor thrust and ρ_∞ is the free-stream density. Figure 5 (left) reports C_T for the four resolution levels. Experimental C_T measured with two different techniques (i.e. pressure from PIV and aerodynamic balance) for varying J are also reported. The uncertainty of the experimental data is about 2%. Since it was verified by de Vries et al.[9] that the presence of the pylon does not affect the C_T, computations without installation effects are not carried out. The figure shows that the C_T increases by using finer grid resolutions. A converging trend with variations lower than 1% between the two finest resolutions levels is found. For this reason, the grid resolution equal to 14 vx$/D_{hole}$ is selected for further validation. The difference with respect to the measured values might be due to the fact that the blade boundary layer is not fully resolved and small differences between the CAD geometry and the experimental one might be present.[40] Additionally, the experimental thrust was obtained as difference of the axial force of the full system and the one in absence of the propeller blades, which is based on the assumption that the propeller motion does not affect the drag of both the nacelle and the sting.[10]

Since the aim of the manuscript is to investigate the propeller-slipstream pylon impingement, the computed propeller wake is validated against the measurements. The radial distribution of the dimensionless total pressure difference $\left(P_{t_{X/c=0.2}} - P_{t_\infty}\right)/P_{t_\infty}$ at $X/c = 0.2$ and $Z/R = 0$ is plotted in Figure 5 (right). A reasonable agreement between experiments and computational results is found. A small kink at $r/R \approx 0.41$ is observed in the computational results and it is attributed to the change of resolution between adjacent VRs. The wake flow is further validated by looking at the iso-contour of the dimensionless stream-wise velocity component U/U_∞ in the X–Y plane at $Z/R = 0$, shown in Figure 6. The figure shows that

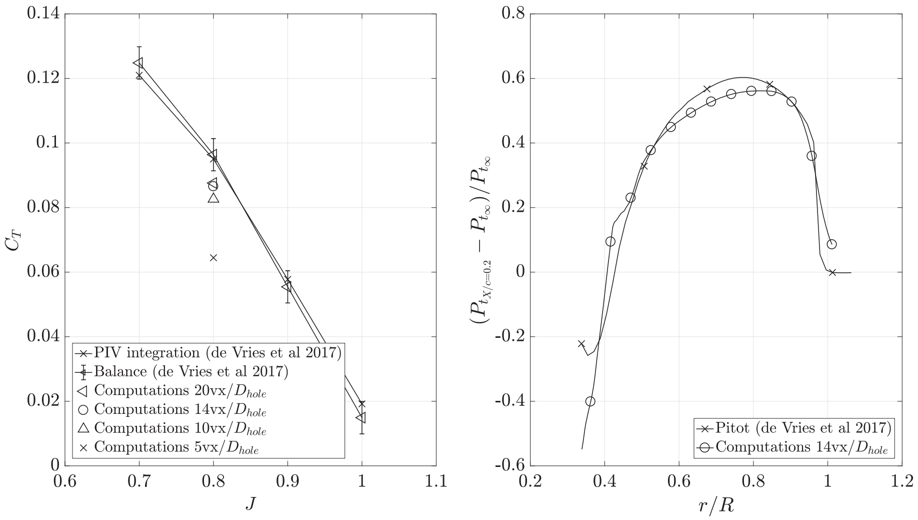

Figure 5. (Left) Thrust coefficient obtained from computations with different resolutions compared with experimental data. (Right) Pressure distribution in the near wake of the propeller at $X/c = 0.2$. Experimental data taken from de Vries et al.[9]

U/U_∞ increases in the wake slipstream reaching a value of about 1.2, which is coherent with the chosen J. As in the experiments, three main regions can be distinguished: the propeller root vortices for $Y/R < 0.5$, the propeller wake for $0.5 < Y/R < 1$ and the tip vortices at $Y/R \approx 1$ with spacing of $0.5\,R$. The axial-velocity component increases for $0.4 < Y/R < 0.8$, while it decreases for $Y/R > 0.8$. This location corresponds to the radial position of maximum loading on the propeller blades.[9]

After having verified that the wake flow is well captured, the root-mean-square of the instantaneous pylon pressure coefficient ($C_{p_{rms}}$) is compared with measurements in Figure 7. The instantaneous pressure coefficient $C_p(X, Y, t)$ is defined as

$$C_p(X, Y, t) = \frac{P(X, Y, t) - P_\infty}{0.5\rho_\infty U_\infty^2} \tag{12}$$

It is worth mentioning that experimental data were obtained by using an additional sleeve, not present in these computations, sliding in the Z direction and equipped with eight microphones per side. An overall good agreement, both in terms of amplitude of the pressure fluctuations and of their spatial distribution is found. The figure shows that the propeller tip vortex, that impinges at $Z/R \approx -1$, is the dominant source of pressure fluctuations over the entire pylon chord. The amplitude of the pressure fluctuations is the largest at the pylon leading edge, and then it slowly decreases towards the trailing edge because of the viscous interaction between the thicker boundary layer and the tip vortex.[8] As shown in Figure 7, the span-wise displacement of the tip vortex is visible; it moves in opposite directions: towards $Z/R < -1$ at retreating side, while towards $Z/R > -1$ at the advancing side. Furthermore, computational results capture the small region near the leading edge on the retreating blade side, directly inboard of the tip vortex impingement location ($Y/R \approx 0.05$, $Z/R \approx -0.95$), with localized low and high magnitude of the surface

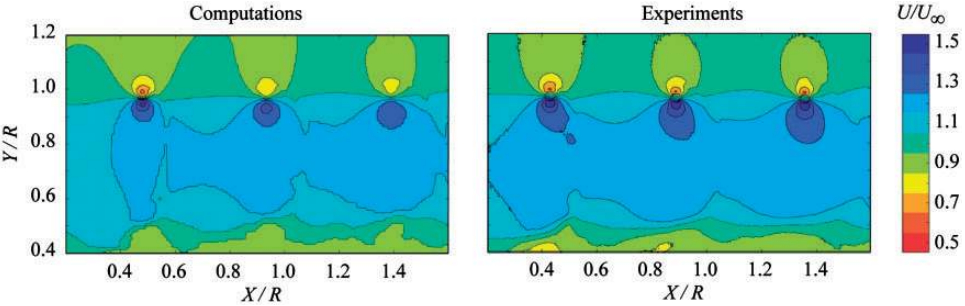

Figure 6. Dimensionless time-averaged stream-wise velocity U/U_∞ at $Z/R = 0$. Experimental data taken from de Vries et al.[9]

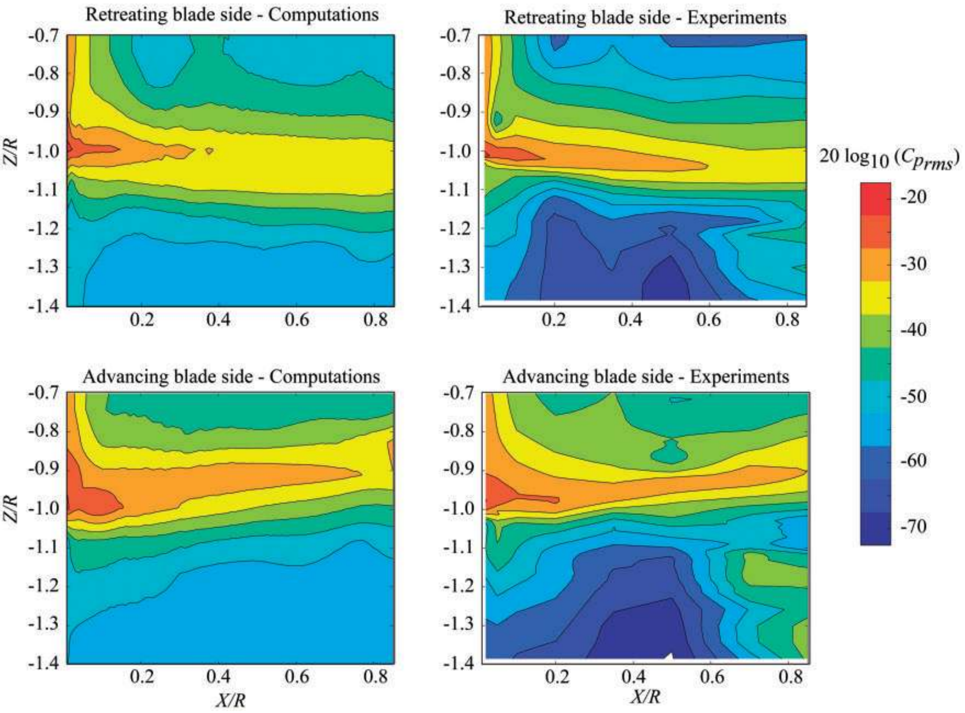

Figure 7. Root-mean-square of the surface pressure fluctuations on the pylon surface. Experimental data taken from de Vries et al.[9]

pressure fluctuations. This is caused by the destructive interference between the pressure perturbations caused by the blade wake and the tip vortices.[10] The opposite occurs on the advancing side, leading to a wider region of high pressure fluctuations. Some differences between computations and experiments are visible for $Z/R < -1.1$, where experiments show lower magnitude of the surface pressure fluctuations with respect to the computations in the central part of the pylon. This might be caused by a local effect of the sleeve in the undisturbed flow region.

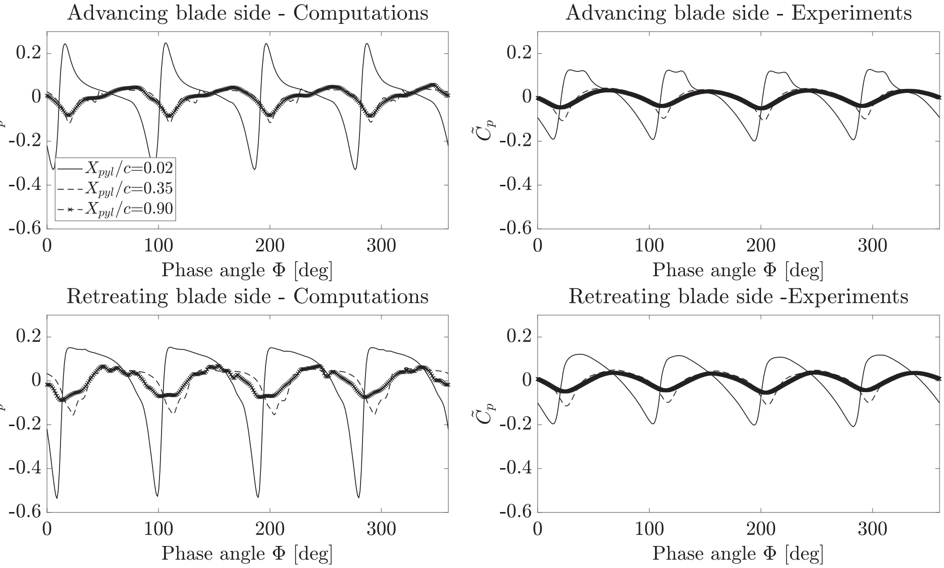

Figure 8. Phase-averaged pressure wave-forms at three stream-wise locations along the tip-vortex trajectory. Experimental data taken from de Vries et al.[9]

Because of the flow periodicity, the comparison is further extended to the phase-averaged wave-forms of the pressure coefficient $\tilde{C}_p$ in Figure 8. The phase angle $\Phi = 0$ corresponds to one of the propeller blades aligned in the Z direction. Three control points along the tip-vortex trajectory on both the retreating and advancing sides are considered at $X_{pyl}/c = 0.02$, 0.35 and 0.90. Data are extracted at radial coordinates $Z/R = -0.992$, –1.025 and –1.034 on the advancing blade side and $Z/R = -0.975$, –0.949 and –0.848 on the retreating blade side. Some differences are present at $X_{pyl}/c = 0.02$ where computations show larger amplitude of both the positive and negative peaks. The reason might be due to the finite size of the sensing area of the microphones, which diameter is three times larger than the smallest voxel close to the pylon surface and to the dampening of the peak within the sensor cavity. At $X_{pyl}/c = 0.35$ and 0.90, the strength of the vortex reduces because of the viscous interaction and no difference is found between experiments and computations. From a physical perspective, the figure shows strong differences between the advancing and retreating sides of the pylon. It is interesting to note that the maximum variation of $\tilde{C}_p$ is constant, meaning that the strength of the vortex does not vary between the two sides. However, the curves are symmetric with respect to 0 on the advancing blade side, while they are not on the retreating blade side. This is due to the fact that the pylon is not aerodynamically symmetric because of the helicoidal motion of the propeller wake.

The aerodynamic asymmetry is confirmed by the time-averaged pressure coefficient C_p shown in Figure 9. In the figure, the experimental C_p is retrieved from PIV at 1.5 mm from the surface for both the solid and flow-permeable leading-edge configurations in the range $0 < X_{pyl}/c < 0.2$. It is relevant to note that strong similarities with the experiments are found also for the flow-permeable leading-edge insert, where the suction peak displaces downstream towards the end of the flow-permeable part at $X_{pyl}/c \approx 0.1$ and increases in magnitude with respect to the solid pylon. Similar modifications of the pressure distribution occur for a clean aerofoil by increasing the profile thickness or by moving the location of the

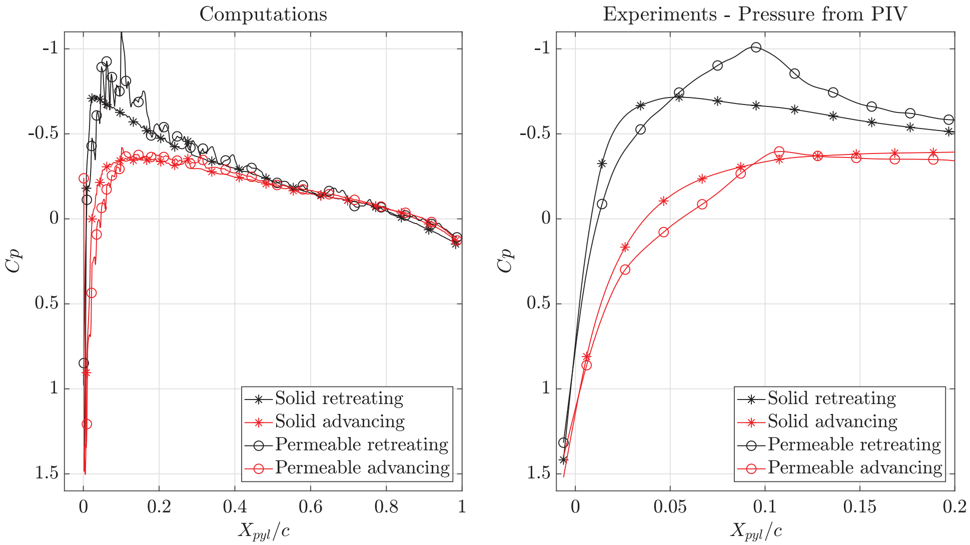

Figure 9. Time-averaged pressure coefficient at $Z/R = -0.74$. Experimental data taken from della Corte et al.[16]

maximum thickness.[41] This is caused by the change of the aerodynamic shape of the pylon (further discussed in the next section) as also observed by Tinetti et al.,[13,14] Mineck and Hartwich[42] and Lee.[15]

The validation results of the acoustic prediction are shown in Figure 10. The convergence of the grid is assessed by comparing noise results for the two finest resolutions tested. Furthermore, the reliability of the FWH computation is further verified by comparing noise results obtained by using both the solid and permeable formulations (Noise computations section). Figure 10 shows the polar plot of the overall sound pressure level (OASPL) obtained using two radial arches of 40 microphones each located at a distance of $4R$ and $Z/R = 0$. Receiver angles ranging between 0°and 180° refer to the advancing blade side, while from 180°to 360° to the retreating blade side. Small variations are found (less than 1 dB) when increasing the resolution. Additionally, the two formulations show almost overlapping results with differences smaller than 0.5 dB. This guarantees that a satisfying level of convergence is reached for the 14 vx/D_{holes} case, which is used for the rest of the study.

Flow-field analysis

Flow-field around the pylon

The three-dimensional flow field is shown in Figure 11 for both the solid (left) and flow-permeable (right) leading-edge configurations. In the figure, iso-surfaces of the λ_2 criterion for vortex identification[43] colour-contoured with the dimensionless velocity magnitude $\mathbf{U}/U_\infty$ are plotted. The figures show the expected features of the flow behind a propeller, i.e. the turbulent wake flow and the propeller tip vortex, as discussed before (Figure 7). The

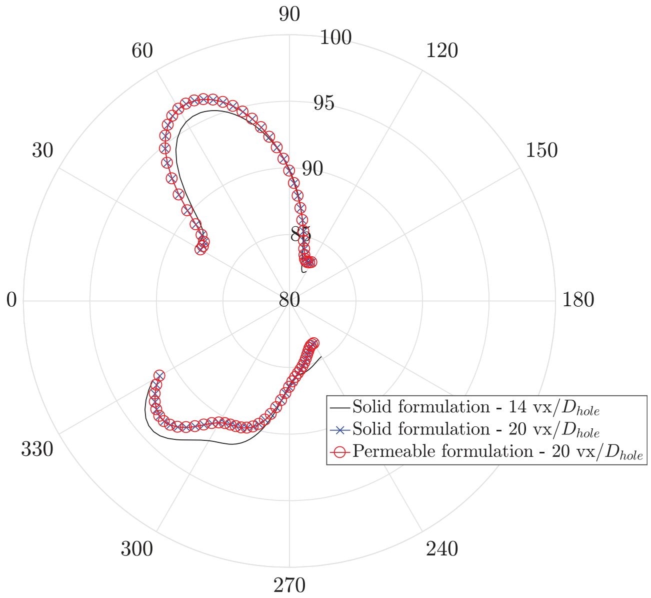

Figure 10. Polar plot of the overall sound pressure level (OASPL). Receiver angles ranging between 0° and 180° refer to the advancing blade side while from 180° to 360° to the retreating blade side.

comparison of the figures highlights the main differences between the two configurations: the generation of a thicker boundary layer over the retreating blade side of the pylon.

Due to the periodicity of the phenomenon, the flow around the pylon is further investigated by means of phase-averaged data in X–Y planes at $Z/R = -0.74$ (i.e. the wake-impingement region) and 0.97 (i.e. the tip-vortex-impingement region). These slices are plotted in Figures 12 and 13, where iso-contour of the phase-averaged dimensionless axial velocity $\tilde{U}/U_\infty$ for both the solid (left) and the flow-permeable (right) leading edges are shown. Only three phase angles equal to $\Phi = 0°$, $9°$, $27°$ are reported for the sake of conciseness. It is reminded that $\Phi = 0°$ is chosen as the phase angle at which one of the blades is oriented along the Z-axis.

In the wake-impingement region (Figure 12), no relevant difference is visible between the three phases. Conversely, the slice extracted at $Z/R = -0.97$ (Figure 13) clearly shows the phase evolution of the tip vortex approaching and impinging on the pylon leading edge. The tip vortex approaches the pylon ($\Phi = 27°$) at an oblique angle, caused by the helicoidal trajectory of the vortex (Figure 11). Because of the flow deceleration close to the pylon leading edge, the vortex bends around the pylon before impinging on it ($\Phi = 0°$). On the advancing blade side ($Y_{pyl}/c > 0$), the pitch angle of the vortex remains similar to that observed before the impingement. The retreating side, on the other hand, displays bending of the vortex due to the acceleration caused by the angle of attack induced by the propwash. After the impingement ($\Phi = 9°$), the low-speed region close to the stagnation point reduces in size and a localized area with higher velocity is generated in its proximity. As the vortex convects downstream, it is split; on the advancing side ($Y_{pyl}/c > 0$), the vortex segment is almost parallel to the pylon. This can be seen from the fact that the region of influence of the vortex is aligned with the chord-wise direction as also visible

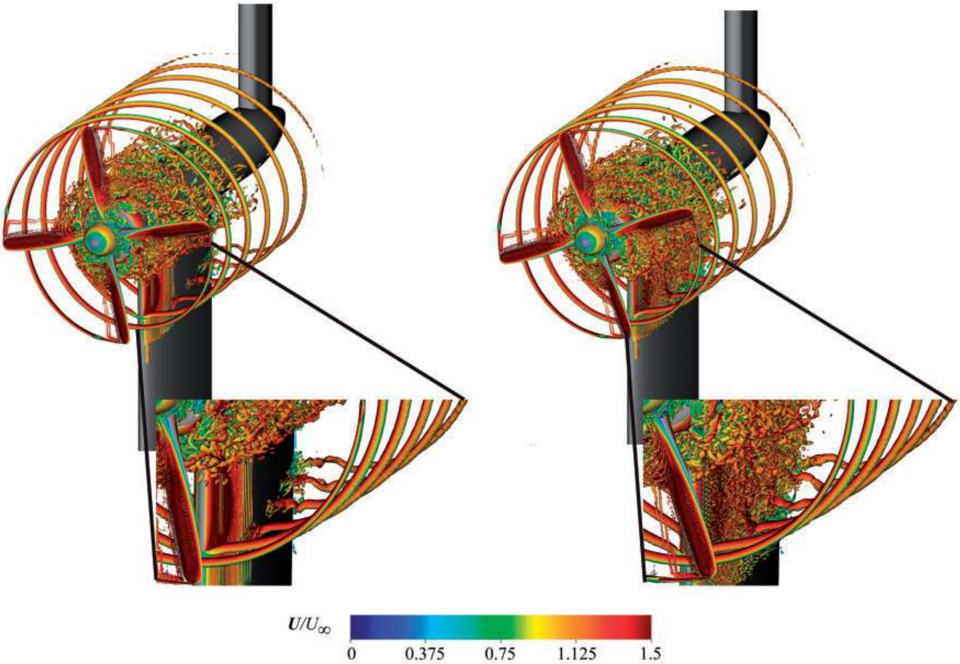

Figure 11. Instantaneous flow field for the solid (left) and flow-permeable (right) leading-edge configurations. Iso-surface of the λ_2-criterion for vortex identification ($\lambda_2 = -2.5 \times 10^6\ \mathrm{s}^{-1}$) colour-contoured with the dimensionless velocity magnitude $\mathbf{U}/U_\infty$.

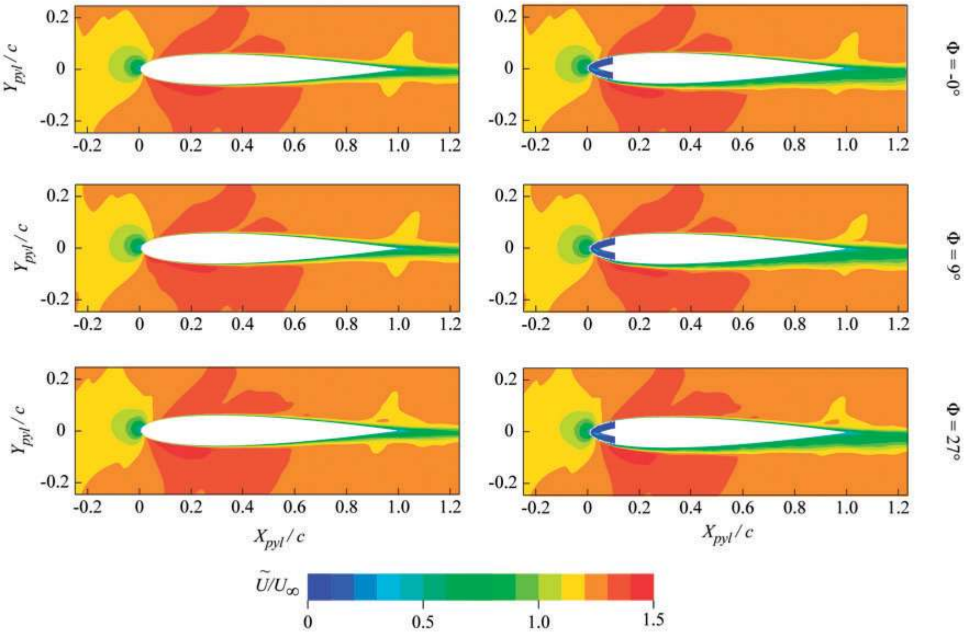

Figure 12. Phase-averaged flow field in the X–Y plane at $Z/R = -0.74$ for the solid (left) and flow-permeable (right) leading-edge configurations.

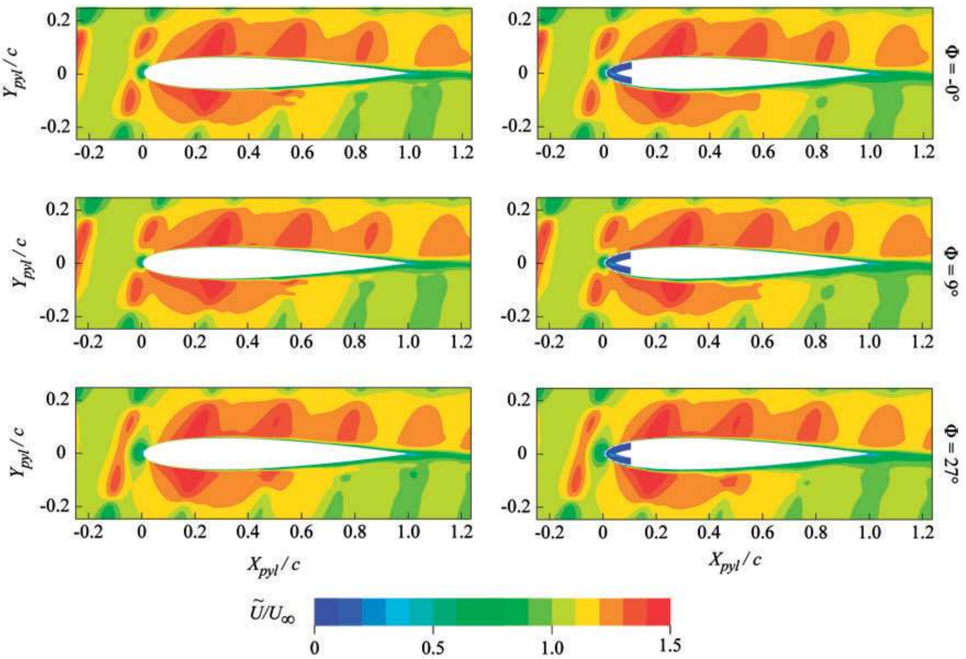

Figure 13. Phase-averaged flow field in the X–Y plane at $Z/R = -0.97$ for the solid (left) and flow-permeable (right) leading-edge configurations.

from Figure 7. The velocities induced by the vortex segment on the advancing side are higher than on the retreating side. This is due to the gradual span-wise displacement of the vortex, which makes the vortex penetrating the plane further on the advancing side than on the retreating side. This span-wise displacement further increases when the vortex continues to convect downstream.

Comparing the solid with the flow-permeable leading-edge, it is evident that, for both the planes and independently on the phase angle, the flow field far from the pylon surface is weakly affected by the leading edge geometry. In particular, the spatial organization and the velocity of the tip vortices are similar. Conversely, the flow near the surface shows a thicker boundary layer over the retreating side of the pylon, while almost no difference is visible on the advancing side. This is quantified in Figure 14, where the dimensionless time-averaged axial velocity profile U/U_∞ in the near wake at $X_{pyl}/c = 1.05$ is plotted. It is evident that, on the advancing blade side ($Y_{pyl}/c > 0$), the curves overlap, thus suggesting that the effect of the rougher surface is negligible. On the other side, the wake deficit is larger for the porous case, thus suggesting the development of an asymmetric wake, as also shown in the experiments. This is visible for both the wake and tip-vortex impingement planes (Figures 12 and 13) and is caused by the cross-flow through the cavity from the advancing to the retreating blade side because of the aerodynamic asymmetry generated by the presence of the propeller (Figure 9). The effect of the cross-flow does not depend on the Z/R plane as also visible from the three-dimensional visualization in Figure 11, thus suggesting that is mainly caused by the helicoidal motion of the propeller wake. The flow within the cavity responsible for these effects is described in the following section.

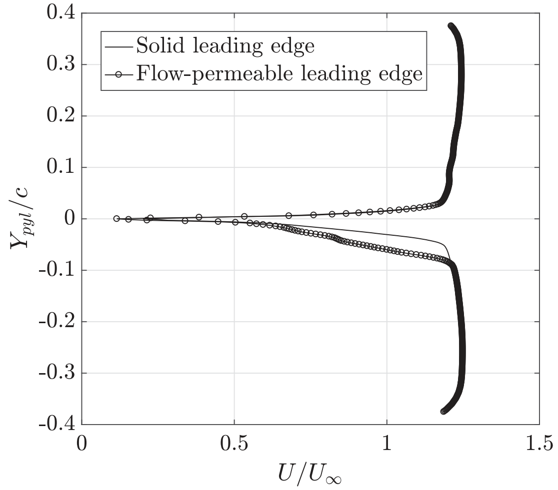

Figure 14. Near-wake time-averaged axial velocity at $X_{pyl}/c = 1.05$ and $Z/R = -0.97$.

As a main consequence of the cross-flow and of the induced turbulent boundary layer on the retreating blade side, the surface pressure fluctuations are different between the solid and the flow-permeable leading-edge configurations. This is shown in Figures 15 and 16 for the advancing and retreating blade sides, respectively. In the figure, the instantaneous fluctuating pressure coefficient (i.e. the instantaneous pressure coefficient to which the mean pressure coefficient is subtracted) $\overline{C}_p'$ is shown. Figure 15 shows that the footprints of the tip vortices on the pylon advancing side are almost identical between the two configurations. The flow-permeable leading edge shows additional turbulent fluctuations localized around the tip-vortex impingement region. Conversely, more evident differences are visible in Figure 16, where the effect of the turbulent flow is localized on the part of the pylon where the flow-permeable leading-edge insert is installed. The footprint of the tip-vortex on the pylon surface is mitigated by its interaction with the turbulent boundary layer.[8] This is evidenced by the smaller peak amplitude in the second half of the pylon chord.

Near- and in-cavity flow organization

The previous section has shown that the main effect of the flow-permeable leading-edge insert is to generate a thicker boundary layer on the retreating blade side because of the cross-flow though the cavity. In this section, the flow within the cavity is described in detail.

The comparison between the two leading-edge inserts is shown by plotting the dimensionless time-averaged velocity components U/U_∞ and V/U_∞ in the X and Y directions, respectively. For the solid leading edge only, a slice at $Z/R = -0.97$ (Figure 17) is shown because no major differences are present in the propeller wake impingement region ($Z/R = -0.74$). Conversely, for the flow-permeable leading-edge insert both planes are shown (Figure 18).

Figure 17 shows that the stagnation point slightly moves toward the advancing blade side and that the vertical velocity is not symmetric between the two sides of the pylon. The

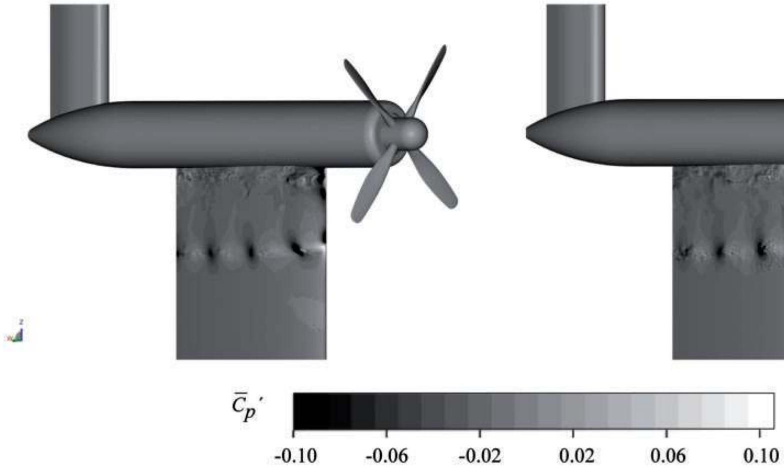

Figure 15. Instantaneous fluctuating pressure coefficient $\overline{C}_p'$ on the pylon advancing side.

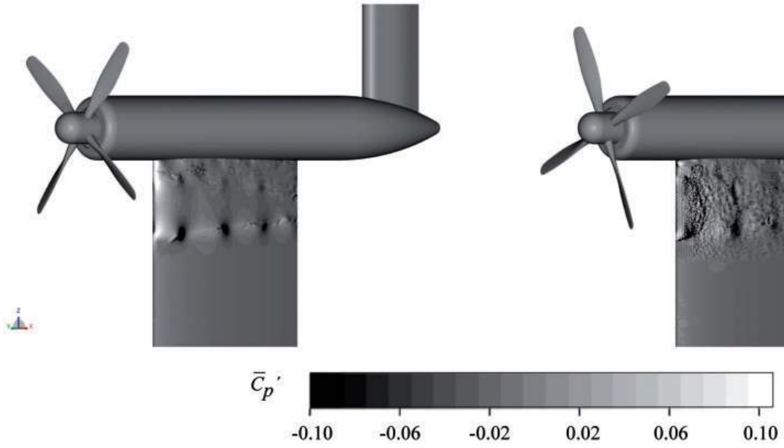

Figure 16. Instantaneous fluctuating pressure coefficient $\overline{C}_p'$ on the pylon-retreating side.

negative vertical velocity region extends upstream more than the positive one, because of the vortex deformation discussed above (Figures 7 and 11). Similar features are visible for the flow-permeable leading-edge insert as shown in Figure 18. In addition, the flow penetrates within the cavity with larger axial velocity through the pores located closer to the stagnation point. Because of the aerodynamic asymmetry of the flow around the pylon, the flow within the cavity goes from the advancing to the retreating side. The relative high-speed region extends towards more downstream locations at $Z/R = -0.97$ with respect to $Z/R = -0.74$. Small recirculation regions, characterized by $U/U_\infty < 0$, are present on both sides of the cavity and for both Z/R planes. Where a larger negative axial velocity is present (e.g. the hole at $X_{pyl} = 0.01$ and $Y_{pyl} = 0.025$), the V/U_∞ velocity component is smaller (i.e. in correspondence of the first hole on the retreating blade side), thus suggesting that the internal

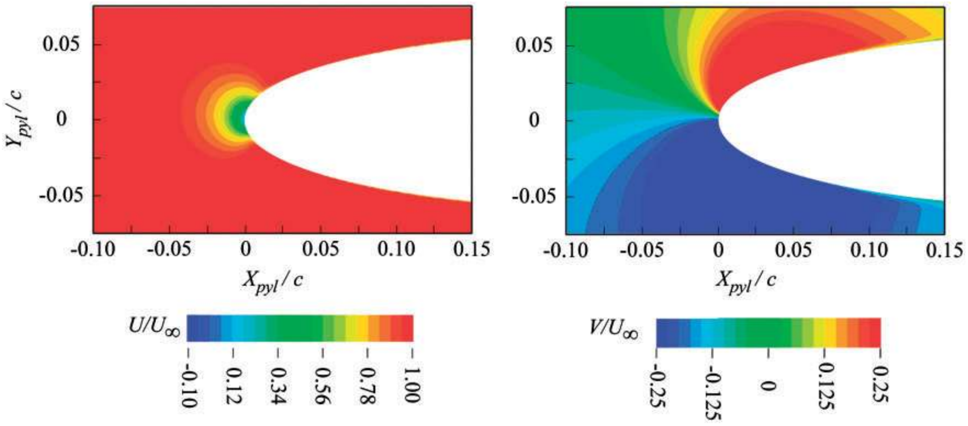

Figure 17. Zoomed view around the leading edge of the time-averaged flow field in the *X*–*Y* plane at $Z/R = -0.97$.

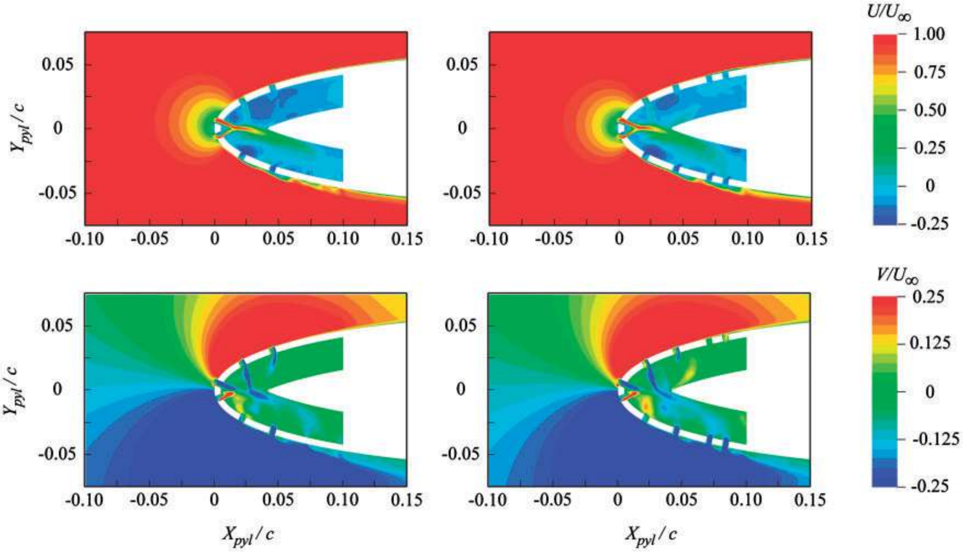

Figure 18. Zoomed view around the leading edge of the time-averaged flow field in the *X*–*Y* plane at $Z/R = -0.74$ (left) and $Z/R = -0.97$ (right).

recirculation acts as a barrier not allowing the flow to exit the cavity. This causes a distributed injection of momentum to the boundary layer over the flow-permeable insert, which causes the thickening of the boundary layer (Figure 6).

In order to get further insights into the effect of the periodic impingement on the cavity flow, phase-averaged data at $Z/R = -0.97$ are plotted for four phase angles ($\Phi = 0°$, $10°$, $36°$ and $54°$) in Figure 19. Both the axial ($\tilde{U}/U_\infty$) and span-wise ($\tilde{V}/U_\infty$) velocity components are plotted on the left and right side of the figure, respectively.

The figure shows that, as expected, the flow continuously enters the cavity. When the vortex approaches the leading edge, the flow is pushed towards the pylon and as soon the vortex passes the leading edge, a stronger recirculation starts within the cavity, that reaches its peak when the vortex has passed the entire flow-permeable region. As a consequence, at the retreating side, the boundary layer shows a periodic growth with maximum when the vortex has fully passed the flow permeable insert.

Acoustic analysis

The previous section has shown that the most relevant effect of the flow-permeable leading edge is to enhance the aerodynamic asymmetry between the two sides of the pylon and to generate a much thicker turbulent boundary layer on the retreating blade side. The reduction of the amplitude of the surface pressure fluctuations on the retreating blade side towards the pylon trailing edge can be beneficial for mitigating structure-borne noise. However, the installation of the flow-permeable leading edge can affect the near-field noise because of the turbulent flow developing over the pylon. In this section, this aspect is investigated by means of the FWH acoustics analogy (see Noise computations section).

Figure 20 shows the polar plot of the OASPL for the two leading-edge configurations obtained using two radial arches of 40 microphones each located at a distance of $4R$ and $Z/R = 0$. Receiver angles ranging between $0^\circ$and 180° refers to the advancing blade side, while from 180° to 360° to the retreating blade side.

The figure shows that, as a consequence of the aerodynamic asymmetry, the directivity plots are asymmetric with respect to the axial direction. Both lobes show peaks oriented in the upstream direction. At the advancing blade side, the lobe shows a peak at a receiver angle of about 60°, while at the retreating blade side, a wider and more uniform lobe is found for receiver angles ranging between 285° and 315°. The installation of the flow-permeable leading edge has two different effects for the two pylon sides: it shows an increase of the OASPL at the advancing blade while, at the retreating blade side, a reduction of the OASPL for receiver angles between 285° and 315°, and an increase for more downstream angles is found. The difference between the two configurations is better shown in Figure 21, where the difference of OASPL between the solid and the flow-permeable configurations is plotted (ΔOASPL). A positive value means that the flow-permeable leading edge reduces noise with respect to the solid configuration. The maximum noise reduction is about 2 dB, while the maximum noise increase is about 1.5 dB. It is interesting to notice that pressure fluctuations increase on one pylon side corresponds to noise reduction on the opposite side.

The previous figure quantifies the near-field noise for the entire system. In order to isolate the effect of the flow-permeable leading edge, the near-field noise is computed by integrating only the surface pressure fluctuations on the pylon. The sound pressure level in 1/12 octave band is plotted in Figure 22 for three receiver angles corresponding to the maximum noise increase, maximum noise reduction and no noise variation of the entire system (Figure 20). Both the advancing and the retreating blade sides are reported with a continuous and dashed line, respectively. In the figure, the frequency is non-dimensionalized with respect to the BPF equal to 848 Hz.

The figure shows the two most relevant effects of the flow-permeable leading-edge insert: the reduction of the tone amplitude and the increase of the broadband component at high frequencies. At the retreating blade side and receiver angle of -52.5°, the flow-permeable leading edge reduces the amplitude of the third and fourth BPF with the peak of the latter

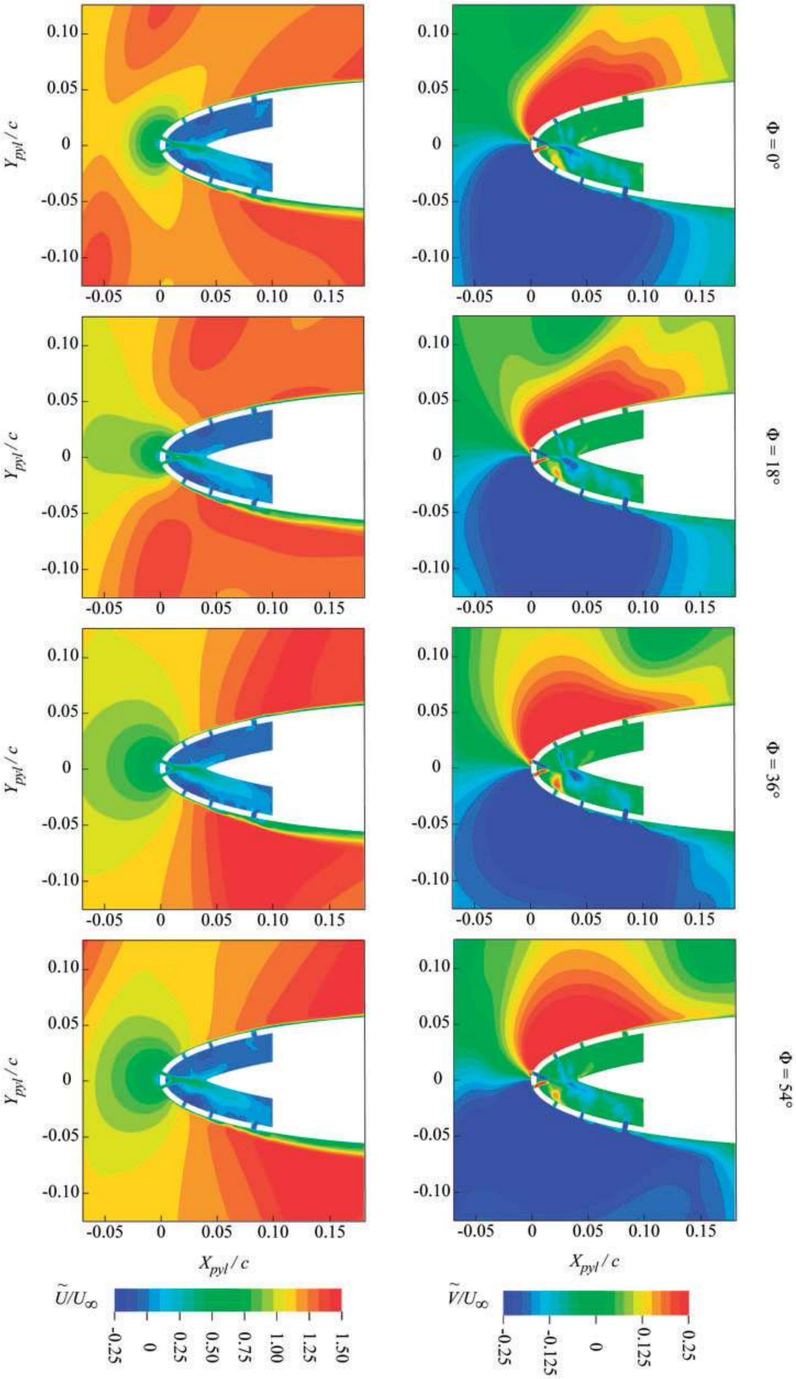

Figure 19. Zoomed view around the leading edge of the phase-averaged flow field at $Z/R = -0.97$.

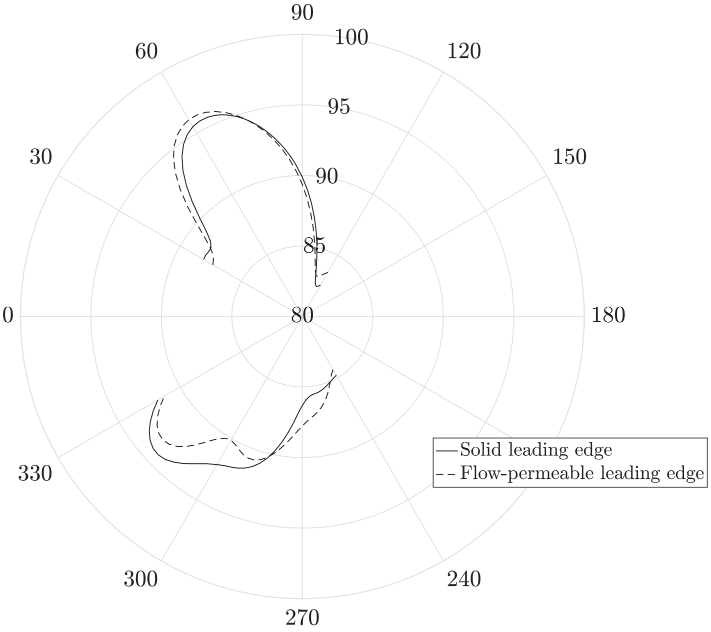

Figure 20. Polar plot of the overall sound pressure level (OASPL) for the two leading-edge configurations. Receiver angles ranging between 0° and 180° refer to the advancing blade side while from 180° to 360° to the retreating blade side.

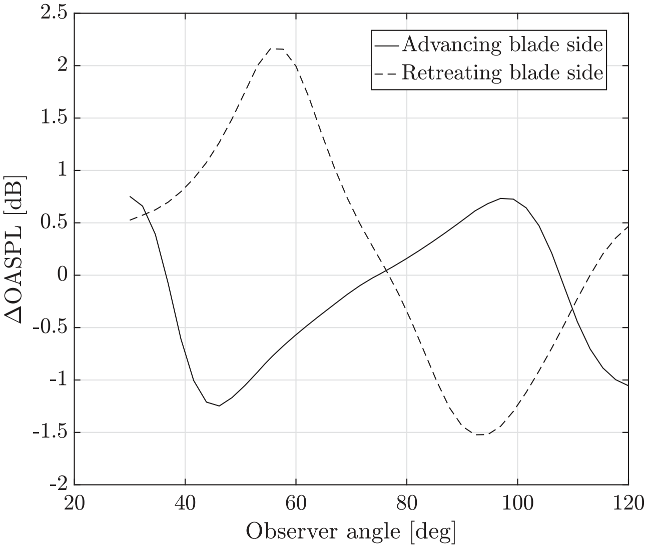

Figure 21. Overall Sound Pressure Level (OASPL) with respect to the solid case. Positive means noise reduction. Receiver angles are reported in absolute values.

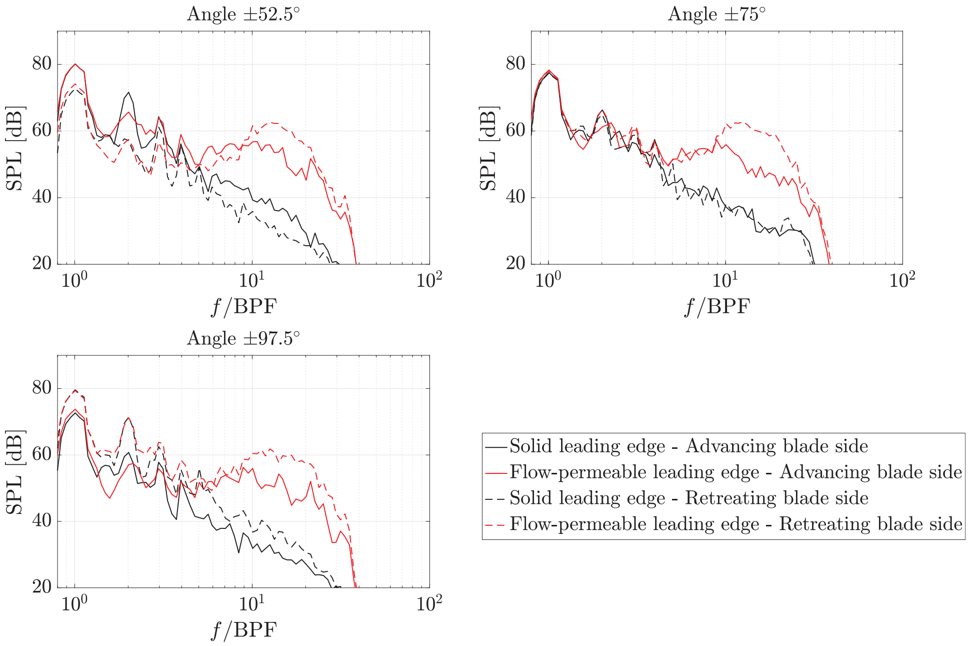

Figure 22. Sound pressure level (SPL) in 1/12 octave band for three receiver angles corresponding to the maximum noise increase, maximum noise reduction and no noise variation of the entire system.

that almost disappears. It has almost no effects of the first two BPFs. For frequencies between the third and the seventh BPF, a reduction of the broadband noise of about 2 dB is found; conversely, for higher frequency, a strong increase of the broadband noise is present. Similar features with similar amplitude and frequency behaviour were also measured with acoustic beamforming. At the same receiver angle but at the advancing blade side, almost no variation, apart a small reduction of the amplitude of the second BPF, is found up to the seventh BPF where the broadband noise increases. Conversely, at the receiver angle of −97.5°, as expected from the flow analysis, the flow-permeable leading edge does not reduce the tones but increases only the broadband part. Finally, acoustic results show that the broadband noise contribution is larger at receiver angles oriented towards downstream locations.

Conclusions

The flow and the acoustic fields of a propeller in tractor configuration are investigated. The configuration is obtained by placing a pylon in the slipstream of the propeller. A solid and a flow-permeable leading-edge configuration are investigated. The computational set-up reproduces the experiments carried out at Delft University of Technology.[9,10,16]

Computational results are validated with a grid convergence study and against experimental data. A good agreement is found between the experiments and the numerical results by comparing the thrust coefficient, the propeller wake, the surface pressure fluctuations for the pylon with the solid leading edge and the pressure coefficient variation between the solid and the flow-permeable configurations.

It is confirmed that the effect of the flow-permeable leading edge is to alter the aerodynamic shape of the pylon showing similar features to the ones that could be obtained using a thicker aerofoil or by moving the location of the maximum thickness, i.e. downstream displacement and increase in magnitude of the suction peak. This is caused by a thicker boundary layer that develops over the retreating blade side of the pylon for the flow-permeable leading-edge insert due to the cross-flow through the cavity. This flow motion is caused by the aerodynamic asymmetry of the pylon due to the helicoidal motion of the wake and causes the drag increase found in the experiments. Conversely, the flow-permeable leading edge has negligible effects on the development of the boundary layer on the advancing blade side. The interaction between the propeller tip vortex and the turbulent boundary layer reduces the amplitude of the surface pressure fluctuations towards the trailing edge of the pylon on the retreating blade side.

The acoustic analysis shows that the installation of the flow-permeable leading-edge insert increases the OASPL up to 1 dB at the advancing blade side, while it reduces the OASPL up to 2 dB at the retreating blade side for receiver angles between 285° and 315°. The effect of the flow-permeable insert is to reduce the amplitude of the tone corresponding to the third and fourth BPF only at the retreating blade side, while it increases the broadband noise for all the receiver angles for frequencies higher than the seventh BPF. Finally, acoustics results confirm that the effect of the turbulent boundary layer developing on the retreating blade side of the pylon is to increase the broadband noise with respect to the solid configuration.

Acknowledgements

The authors would like to thank Dr. Wouter C.P. van der Velden for the useful suggestions about the computational set-up and Tomas Sinnige, Biagio Della Corte and Reynard de Vries for the useful discussions and for providing the experimental data.

Declaration of conflicting interests

The author(s) declared no potential conflicts of interest with respect to the research, authorship, and/or publication of this article.

Funding

The author(s) received no financial support for the research, authorship, and/or publication of this article.

References

1. Mann S and Stuart C. Advanced propulsion through the 1990s – an airframer's view. In: *21st Joint propulsion conference*, Monterey, CA, 8–11 July 1985, AIAA 1985–1192. American Institute of Aeronautics and Astronautics.
2. Goldsmith I and Bowles J. Potential benefits for propfan technology on derivatives of future short- to medium-range transport aircraft. In: *16th Joint propulsion conference*, Hartford, CT, 30 June–2 July 1980, AIAA 80-1090. American Institute of Aeronautics and Astronautics.
3. Block P. Experimental study of the effects of installation on single and counter-rotation propeller noise. Technical report, NASA – 2541, 1986.

4. Block P. Directivity and trends of noise generated by a propeller in a wake. Technical report, NASA – 2609, 1986.
5. Magliozzi B, Hanson D and Amiet R. Propeller and propfan noise. In: *Aeroacoustics of flight vehicles: theory and practice*. volume 1: Noise S. Hampton, VA: NASA Langley Research Center, 1991, pp.1–64.
6. Martinez R. Predictions of unsteady wing and pylon forces caused by propeller installation. Technical report, NASA Contractor Report – 178298, 1987.
7. Ljunggren S, Samuelsson I and Widig K. Slipstream-induced pressure fluctuations on a wing panel. *J Aircraft* 1989; 26: 914–919.
8. Johnston RT and Sullivan JP. Unsteady wing surface pressures in the wake of a propeller. *J Aircraft* 1992; 30: 644–651.
9. de Vries R, Sinnige T, Della Corte B, et al. Tractor propeller-pylon interaction, part I: characterization of unsteady pylon loading. In: *AIAA SciTech Forum, 55th AIAA Aerospace Sciences Meeting*, Grapevine, TX, 9–13 January 2017, AIAA 2017–1175. American Institute of Aeronautics and Astronautics.
10. Sinnige T, de Vries R, Della Corte B, et al. Unsteady pylon loading caused by propeller-slipstream impingement for tip-mounted propellers. *J Aircraft* 2018; DOI: 10.2514/1.C034696
11. Loeffler I. Structureborne noise control in advanced turboprop aircraft. In: *25th Aerospace sciences meeting*, Reno, NV, 24–26 March 1987, AIAA 1987–1530. American Institute of Aeronautics and Astronautics.
12. Unruh J. Aircraft propeller induced structure-borne noise. Technical report, NASA Contractor Report 4255, 1989.
13. Tinetti A, Kelly J, Bauer S, et al. On the use of surface porosity to reduce unsteady lift. In: *15th AIAA computational fluid dynamics conference*, Anaheim, CA, 11–14 June 2001, AIAA 2001–2921. American Institute of Aeronautics and Astronautics.
14. Tinetti A, Kelly J, Thomas R, et al. Reduction of wake-stator interaction noise using passive porosity. In: *40th AIAA aerospace sciences meeting & exhibit*, Reno, NV, 14–17 January 2002, AIAA 2002–1036. American Institute of Aeronautics and Astronautics.
15. Lee S. Reduction of blade-vortex interaction noise through porous leading edge. *AIAA J* 1994; 32: 480–488.
16. Della Corte B, Sinnige T, de Vries R, et al. Tractor propeller-pylon interaction, part II: mitigation of unsteady pylon loading by application of leading-edge porosity. In: *AIAA SciTech forum, 55th AIAA Aerospace Sciences Meeting*, Grapevine, TX, 9–13 January 2017, AIAA 2017–1176. American Institute of Aeronautics and Astronautics.
17. Roger M, Schram C and De Santana L. Reduction of airfoil turbulence-impingement noise by means of leading-edge serrations and/or porous material. In: *19th AIAA/CEAS aeroacoustics conference*, Berlin, Germany, 27–29 May 2013, AIAA 2013–2108. American Institute of Aeronautics and Astronautics.
18. Roger M and Moreau S. Airfoil turbulence-impingement noise reduction by porosity or wavy leading-edge cut: experimental investigations. In: *INTER-NOISE*, Hamburg, Germany, 21–24 August 2016, pp.6006–6015.
19. Ffwocs Williams J and Hawkings D. Sound generation by turbulence and surfaces in arbitrary motion. *Philos Trans R Soc London A: Math Phys Eng Sci* 1969; 264: 321–342.
20. Mann A, Perot F, Kim MS, et al. Characterization of acoustic liners absorption using a Lattice-Boltzmann method. In: *19th AIAA/CEAS aeroacoustics conference*, Berlin, Germany, 27–29 May 2013, AIAA 2013–2271. American Institute of Aeronautics and Astronautics.
21. Casalino D, Ribeiro A, Fares E, et al. Lattice-Boltzmann aeroacoustic analysis of the LAGOON landing-gear configuration. *AIAA J* 2014; 52: 1232–1248.
22. Khorrami M, Fares E and Casalino D. Towards full aircraft airframe noise prediction: Lattice Boltzmann simulations. In: *20th AIAA/CEAS aeroacoustics conference*, Atlanta, GA, 16–20 June 2014, AIAA 2014–2481. American Institute of Aeronautics and Astronautics.

23. Casalino D, Hazir A and Mann A. Turbofan broadband noise prediction using the Lattice Boltzmann method. *AIAA J* 2017; 56: 609–628.
24. Sanjosé M, Moreau S, Pestana M, et al. Effect of weak outlet-guide-vane heterogeneity on rotor-stator tonal noise. *AIAA J* 2017; 55: 3440–3457.
25. Succi S. *The Lattice Boltzmann equation for fluid dynamics and beyond*. 1st ed. Oxford: Clarendon Press, 2001.
26. Shan X, Yuan XF and Chen H. Kinetic theory representation of hydrodynamics: a way beyond the Navier-Stokes equation. *J Fluid Mech* 2006; 550: 413–441.
27. Chen S and Doolen G. Lattice Boltzmann method for fluid flows. *Annu Rev Fluid Mech* 1998; 30: 329–364.
28. Chen H, Chen S and Matthaeus W. Recovery of the Navier-Stokes equations using a lattice-gas Boltzmann method. *Phys Rev A* 1992; 45: R5339–R5342.
29. Bhatnagar PL, Gross EP and Krook M. A model for collision processes in gases. I. Small amplitude processes in charged and neutral one-component systems. *Phys Rev* 1954; 94: 511–525.
30. Yakhot V and Orszag S. Renormalization group analysis of turbulence. I. Basic theory. *J Sci Comput* 1986; 1: 3–51
31. Lew PT, Najafiyazdi A and Mongeau L. Numerical simulation of sound from flow over an airfoil with a blunt trailing edge. In: *16th AIAA/CEAS aeroacoustics conference*, Stockholm, Sweden, 7–9 June 2010, AIAA 2010–3879. American Institute of Aeronautics and Astronautics.
32. Teixeira C. Incorporating turbulence models into the Lattice-Boltzmann method. *Int J Mod Phys C* 1998; 9: 1159–1175.
33. Wilcox D. *Turbulence modelling for CFD*. 3rd ed. California: DCW Industries, Incorporated, 2006.
34. Launder B and Spalding D. The numerical computation of turbulent flows. *Comput Meth Appl Mech Eng* 1974; 3: 269–289.
35. Brès G, Pérot F and Freed D. A Ffowcs Williams-Hawkings Solver for Lattice-Boltzmann based computational aeroacoustics. In: *16th AIAA/CEAS aeroacoustics conference*, Stockholm, Sweden, 7–9 June 2010, AIAA 2010–3711. American Institute of Aeronautics and Astronautics.
36. Farassat F and Succi G. A review of propeller discrete frequency noise prediction technology with emphasis on two current methods for time domain calculations. *J Sound Vibr* 1980; 71: 399–419.
37. Najafi-Yazdi A, Bres G and Mongeau L. An acoustic analogy formulation for moving sources in uniformly moving media. *Proc R Soc A: Math Phys Eng Sci* 2010; 467: 144–165.
38. Casalino D. An advanced time approach for acoustic analogy predictions. *J Sound Vibr* 2003; 261: 583–612.
39. Curle N. The influence of solid boundaries upon aerodynamic sound. *Proc R Soc A: Math Phys Eng Sci* 1955; 231: 505–514.
40. Ragni D, van Oudheusden B and Scarano F. 3D pressure imaging of an aircraft propeller blade-tip flow by phase-locked stereoscopic PIV. *Exp Fluids* 2012; 52: 463–477.
41. Abbott I and Von Doenhoff A. *Theory of wing sections: including a summary of airfoil data*. New York: Dover Publications, 1999.
42. Mineck R and Hartwich P. Effect of full-chord porosity on aerodynamic characteristics of the NACA 0012 airfoil. Technical report, NASA Technical Paper 3591, 1996.
43. Jeong J and Hussain F. On the identification of a vortex. *J Fluid Mech* 1995; 285: 69.